EUROPEAN ORGANIZATION FOR NUCLEAR RESEARCH
European Laboratory for Particle Physics

Large Hadron Collider Project

LHC Project Report 398

BEAM LOSSES FAR DOWNSTREAM OF THE HIGH LUMINOSITY INTERACTION POINTS OF LHC

I. Ajguirei[1] , I. Baichev[1] and J.B. Jeanneret[2]

Abstract

We consider proton-proton collisions in LHC in which one proton at least leaves the collision point with a small longitudinal momentum transfer. The rate of these events at the nominal luminosity of LHC can induce quenches in some superconducting magnets of the downstream part of the straight-section and of the dispersion suppressor. We propose a safe local collimation scheme and present the residual impact on the cryogenic load.

1 IHEP, Protvino, Russia
2 SL Division, CERN, Geneva, Switzerland

Presented at the Seventh European Particle Accelerator Conference (EPAC 2000)
26-30 June 2000, Vienna, Austria

Administrative Secretariat
LHC Division
CERN
CH - 1211 Geneva 23
Switzerland

Geneva, 14 August 2000

Beam losses far downstream of the high luminosity interaction points of LHC

I. Ajguirei and I. Baichev, IHEP, Protvino, Russia and J.B. Jeanneret, CERN, Geneva, Switzerland

Abstract

We consider proton-proton collisions in LHC in which one proton at least leaves the collision point with a small longitudinal momentum transfer. The rate of these events at the nominal luminosity of LHC can induce quenches in some superconducting magnets of the downstream part of the straight-section and of the dispersion suppressor. We propose a safe local collimation scheme and present the residual impact on the cryogenic load.

1 INTRODUCTION

The products of proton-proton collisions in LHC are basically of three kinds. Most of the particles which are issued from inelastic collisions have a low momentum and a large emission angle compared to the beam. They can be absorbed by specific absorbers placed outside the vacuum chambers. Elastically scattered protons have small angular and momentum deviations and stay inside the acceptance of the ring. In between these two cases, inelastic diffractive protons can induce significant losses in the straight section and the dispersion suppressor which are located immediately downstream of the interaction point. We show that these particles cannot be intercepted by static absorbers but need mobile collimators inside the vacuum chambers. In Section 2, we discuss forward proton differential cross-sections. In Section 3, we present the basic layout of collision straight sections . The method of simulation used to get loss maps are discussed in Section 4. We compare local diffractive loss rates to quench limits and power deposition in cryogenic magnets in Section 6. An intermediate report of the present study was issued in 1999 [1].

2 FORWARD INTERACTIONS

A phenomenological differential cross-section of the reaction $pp \to pX$, in which X represents all possible final states of fragmentation of one of the colliding protons, was taken in [2, 3]. The protons in the final state suffer a slight transverse kick and a large relative momentum offset δ_p which peaks near the beam momentum. Below, s is the center of mass energy squared, $x_F \approx 1 - \delta_p$ the Feynman variable, $q^2 = -t$ the 4-momentum transfer, P stands for a Pomeron particle and R for a Regge trajectory. The cross section of single-diffraction (SD) cover the range $x_F > 0.95$ and is usually described by the PPP and PPR terms of the triple-Regge expansion. In [2] these terms are respectively

$$\frac{d^3\sigma}{dq^2 dx_F} = \left(2.32e^{-3.94q^2} + 0.33e^{-1.12q^2}\right)(1-x_F)^{0.72q^2-1}$$

$$\frac{d^3\sigma}{dq^2 dx_F} = \left(0.95e^{0.01q^2} + 3.47e^{-4.41q^2}\right)\frac{(1-x_F)^{0.72q^2-1.5}}{\sqrt{s}}$$

The Regge expansion is also used to describe non-diffractive (ND) inclusive cross sections down to $x_F = 0.7$.

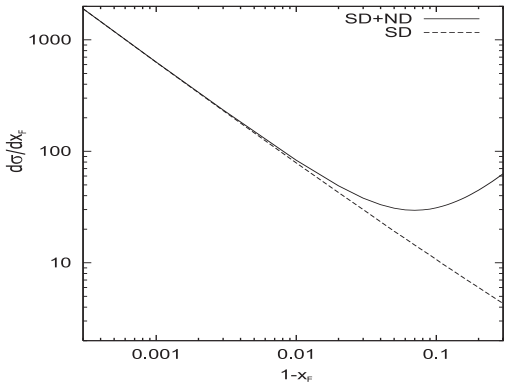

Figure 1: The Differential cross-sections of the inclusive reaction $pp \to pX$ as the sum of the four terms discussed in the text with the ordinate in mbarns. The integral of $d\sigma/dx_F$ between $x_F = [0.7, 0.99]$ is equal to 12.3 mbarns.

We add respectively the $\pi\pi P$ and RRP terms from [3]

$$\frac{d^3\sigma}{dq^2 dx_F} = 19\pi q^2 \frac{(1-x_F)^{1+0.6q^2}}{(m_\pi^2+q^2)^2} e^{-4.3q^2}$$

$$\frac{d^3\sigma}{dq^2 dx_F} = 3.3\pi(1-x_F)^{1.5q^2} e^{0.38q^2}\,.$$

Integrated over q^2, the summed cross section $d\sigma/dx_F$ is shown in Fig. (1). These formulae were compared by their authors with the results of fixed target experiments and partly with results at the CERN ISR. The data at the highest energy today are the results of the CDF collaboration. In a recent work [4] a differential cross-section of the reaction $\bar{p} \to \bar{p}X$ is extracted from these data, which we compare to the sum of the four cross-sections given above in Fig. 2. The agreement at the center of mass energy of $\sqrt{s} = 1800$ GeV shows that the very weak scaling with s in the above formulae might reasonably be used up to 14 TeV.

3 LAYOUT OF COLLISION SECTIONS

The layout of the LHC collision areas is presented schematically in Fig. 3. Downstream the collision point (IP), three final focus quadrupoles (Q1-3) are followed by two dipoles magnets (D1 and D2) which bring the beams to their respective channels in the two-in-one magnets, separated by 194 mm. The cold D2 magnet is protected from neutral and low-momentum charged secondary particles by the fixed TAN absorber which has an aperture similar to D2. With the condition of dispersion $(D^*, D'^*) = (0, 0)$ at the crossing point, the nominal dispersion grows linearly between D1 and D2 and is equal to $D = 97$ mm at D2. Beyond D2, the straight section contains four quadrupoles (Q4-7). Beyond Q7, the dispersion suppressor and the arc form a

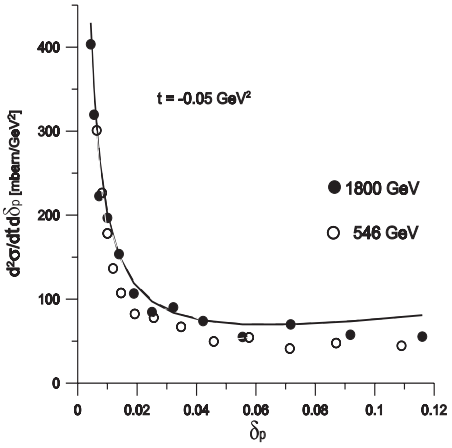

Figure 2: Cross-section of the inclusive reaction $pp \to pX$ (line) compared to the $p\bar{p}$ data at 0.55 and 1.8 TeV (dots).

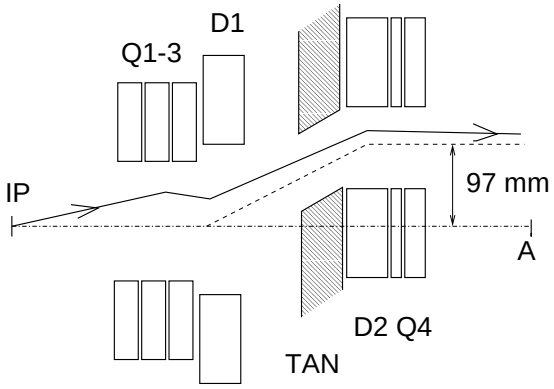

Figure 3: A schematic view of a collision insertion,see text. The second beam channel, not drawn, is obtained by a mirror image around the central axis $IP - A$.

continuous structure of main dipoles and quadrupoles, and the dispersion grows up to $D = 2.2$ m. To avoid parasitic collisions and long-range beam-beam effects, the two beams cross with an angle, and therefore the trajectories do not coincide with the nominal central orbit. This is sketched in Fig. 3 with a crossing angle in the horizontal plane (IP5). To cancel beam-beam linear tune-shift, the crossing plane is vertical in IP1 [5]. These offset trajectories in the quadrupoles introduce a parasitic dispersion, thus making the relative aperture of TAN and D2 to vary with δ_p. This reduces the protection of D2 with vertical crossing, see below and Fig. 4. The transverse offset of the beam in the strong final focus quadrupoles generates a non-negligeable parasitic dispersion (~ 50 mm at D2) for the large momentum offset of the diffracted protons. In addition, the dispersion is non-linear with δ_p (~ 50 % of the linear one at $\delta_p = 0.2$). In the present study, the TAN is located 30 m upstream of D2.

4 TRACKING METHOD

With the complicated geometry described above, a Monte-Carlo method is needed to produce impact maps of diffracted protons onto the coil of the cold magnets. To treat correctly the non-linear optical functions at large δ_p we use the STRUCT code [6] which tracks with using momentum dependent transfer matrices, which are computed for every particle. The lattice and the crossing scheme [5] correspond to the version 6.1 of the LHC optics.

5 BASIC NUMBERS

The differential rates are obtained with the relation

$$\frac{d^3N}{dq^2dx_F} = \mathcal{L} \cdot \frac{d^3\sigma}{dq^2dx_F} . \qquad (1)$$

Our calculations are made with the nominal LHC luminosity of $\mathcal{L} = 10^{34}$ cm^{-2}s^{-1}. We consider protons with $\delta_{p,min} < \delta_p < \delta_{p,max}$ as candidates to be lost downstream of TAN and up to the first adjacent arc cell beyond which the optics is periodic. The first noticeable aperture limitation downstream of the IP occurs at the TAN absorber. With the horizontal half-aperture r = 26 mm and horizontal dispersion $D_x \approx 100$ mm at the TAN we get $\delta_{p,max} \approx 0.25$. In the arcs, D_{max} = 2.2 m and r = 22 mm, then $\delta_{p,min}$ = 0.01. The protons with $\delta_{p,min} < 0.01$ are candidates for an interception by the momentum cleaning system in IR3.

6 RATES AND QUENCH LIMITS

The quench limit in LHC magnets cooled with superfluid helium at $T = 1.9$ K is estimated to $8 \cdot 10^6$ protons m^{-1}s^{-1} or equivalently to a local peak power deposition in the coil $P_q = 5$ mW/cm^3 [7, 8]. Part of the insertion magnets are cooled in a static bath of helium at $T = 4$ K, with a not well known quench limit, but similar to P_q. The longitudinal map of losses in the cryostat of D2, which also contains a bloc of magnetic correctors and Q4 is presented in Fig. 4. The loss density at the entrance of D2 exceeds strongly the quench limit in IR1 but it is below the limit in IR5. The quench limit is met in the correctors in both areas. It is met also in Q5 and the dispersion suppressors in both IR1 and IR5. A dependence of the loss rate with orbit or magnet displacement is also shown in Fig. 5. In all cryostats, the integrated power deposition shown in Table 1 is high. To decrease both the peak loss rates and the integrated power deposition, we introduced collimators. Tracking was made again, followed by a refined scattering algorithm taking into account edge scattering [9] and by shower development with the MARS'98 code [10]. A first collimator is needed in front of D2, to protect D2,Q4 and Q5. It does not protect the dispersion suppressor for which a second one is needed in front of Q5. With one meter long copper collimators located at 15 r.m.s beam units, the peak power loss at D2 in IR1 drops from $P^{max} = 65$ mW/cm^3 down to

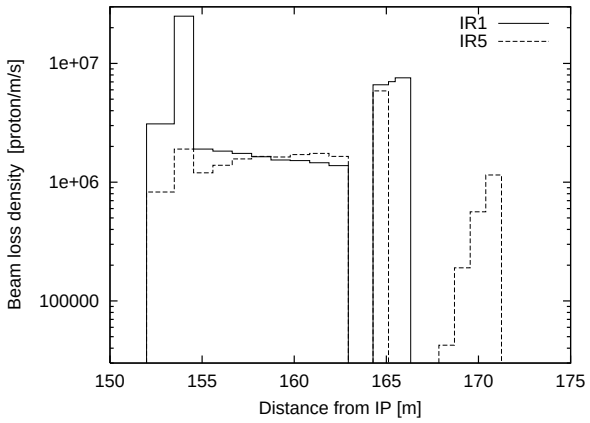

Figure 4: The beam loss density in the region D2-Q4 of IR1 (vertical crossing plane) and IR5 (horizontal crossing plane) at the nominal luminosity $10^{34}\ \mathrm{cm}^{-2}\mathrm{s}^{-1}$. D2 starts at 153.5 m, DH.Q4 and DV.Q4 are located around 165 m and Q4 starts at 167.85 m.

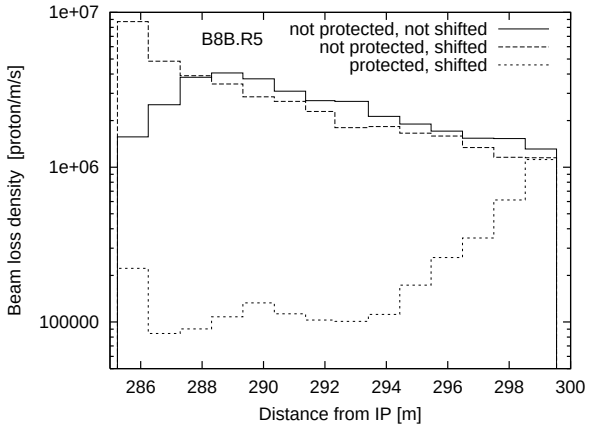

Figure 5: The beam loss density in the dipole B8B of the dispersion suppressor of IR5 at the nominal luminosity. Solid histogram: no collimators in the straight section and perfect alignment of B8B. Dashed histogram: same but with transverse displacement (Δx=4mm, Δy=4mm) of B8B. Dotted histogram: displaced B8B and collimator at Q5. IR1 data are very similar.

$P^{max} \simeq 2\ \mathrm{mW/cm}^3$, as shown in Fig.6. This value is below the quench limit but not much. Further improvement might consist in adding a fixed absorber inside the cryostat in front of the coil. In IR5, the peak density drops down to a safe level of $P^{max} = 0.2\ \mathrm{mW/cm}^3$. At Q5 and in the dispersion suppressor the levels are safe everywhere, see Fig. 5. The integrated power deposition in the cryostats shown in Table 1 are also substantially reduced. The TAN has recently been moved at 13 m upstream of D2. Our numbres must be reevaluated. The peak of losses at the entrance of D2 will be somewhat reduced but no change will occur near the correctors.

7 CONCLUSIONS

Near high luminosity interaction points, movable collimators are needed to prevent quenches of the superconducting magnets in the beam sections located downstream of high luminosity points. They also reduce substantially the cryogenic load, from 120 W down to 35 W per side at each crossing point.

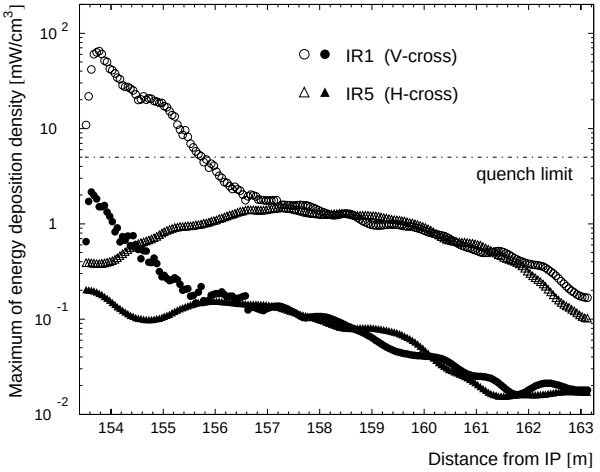

Figure 6: Longitudinal distribution of the density of energy deposition in the hottest sector along the D2 coil, with a radial resolution of 2 mm. Empty symbols: without collimator, solid ones: with collimator at D2.

Table 1: Integrated power deposition in Watt in the different cryostat without collimator and with collimators at D2 and Q5 respectively.

	No collimator		*Collimator at D2 and Q5*	
	H-cross	V-cross	H-cross	V-cross
D2	19	44	~ 2	~ 4
Q5	30	12	~ 3	~ 1
DS	70	50	30	24
Sum	120	110	35	30

8 REFERENCES

[1] I. Baishev, J.B. Jeanneret and G.R. Stevenson, LHC Project Note 208, October 1999.
[2] Field R.D., Fox G.S., Nucl.Phys.B80, 1974, p.367.
[3] Barashenkov V.S. and Slavin N.V., Acta Phys.Polon.B10, 1981, p.563-573.
[4] K. Goulianos and J. Montanha, Phys.Rev.D59(1999), 114017, p.1.
[5] O. Bruning, W. Herr and R. Ostojic, LHC Project Report 315, November 1999.
[6] I. Baishev, A. Drozhdin and N. Mokhov, SSCL-MAN-0034, Dallas, March 1994.
[7] J.B. Jeanneret et al, CERN LHC project report 44,1996.
[8] N. Catalan Lasheras et al., CERN LHC Report 156, 1997.
[9] I. Baishev, Preprint IHEP 87-147, Serpukhov, 1987.
[10] I.L. Azhgirey, I.A. Kurochkin and V.V. Talanov, Annotations of XV Workshop on Charg. Part. Accel., p.74, Protvino, 22-24.10.96.